Changes in the crystallization sequence upon sulfur addition in the $Zr_{52.5}Cu_{17.9}Ni_{14.6}Al_{10}Ti_5$ bulk metallic glass-forming liquid revealed by *in situ* high-energy x-ray diffraction

Benedikt Bochtler,[1,2,*] Jessica Marcela Mariño-Salguero,[3] Alexander Kuball,[1,2] Oliver Gross,[1,2] Fan Yang,[4] Andreas Meyer,[4] Thomas Buslaps,[5] Uta Rütt,[6,7] and Ralf Busch[1]

[1]*Chair of Metallic Materials, Saarland University, Saarbrücken 66123, Germany*
[2]*Amorphous Metal Solutions GmbH, Homburg 66424, Germany*
[3]*Technical University of Darmstadt, Darmstadt 64293, Germany*
[4]*Institute of Materials Physics in Space, German Aerospace Center (DLR), Köln 51147, Germany*
[5]*ESRF – The European Synchrotron Radiation Facility, Grenoble 38000, France*
[6]*Deutsches Elektronen-Synchrotron DESY, Hamburg 22607, Germany*
[7]*Advanced Photon Source, Argonne National Laboratory, Lemont 60439, Illinois USA*

(Received 21 May 2021; accepted 5 October 2021; published 28 October 2021)

Bulk metallic glasses (BMGs) surpass the strength of steels and possess the elasticity and formability of polymers. The key to obtain these properties is to conserve the amorphous structure of a metallic melt and avoid crystallization during processing. In this work, a change in the crystallization sequence in the widely used BMG $Zr_{52.5}Cu_{17.9}Ni_{14.6}Al_{10}Ti_5$ (Vit105) upon the addition of sulfur ($Zr_{51.45}Cu_{17.54}Ni_{14.31}Al_{9.8}Ti_{4.9}S_2$; Vit105 S_2) is revealed by *in situ* high-energy x-ray diffraction, both upon heating from the glassy state and upon cooling from the liquid state during electrostatic levitation. This methodology proves to be a powerful tool to elucidate the complete crystallization behavior of complex BMG-forming liquids. The experiments show that the addition of sulfur changes the crystallization sequence and phases in a different manner upon cooling from the liquid state than upon heating from the glassy state. The thermal stability at low temperatures upon heating is increased, as the supercooled liquid region is extended from 60 to 77 K and the glass transition temperature increases from 671 to 692 K. However, the thermal stability is decreased upon cooling, causing a reduced glass-forming ability.

DOI: 10.1103/PhysRevMaterials.5.103402

I. INTRODUCTION

One of the most used bulk metallic glasses (BMGs) for industrial applications is the Zr-based alloy $Zr_{52.5}Cu_{17.9}Ni_{14.6}Al_{10}Ti_5$ (Vit105). It combines excellent mechanical properties [1–5] with a high glass-forming ability (GFA) [6–8], making it easy to process and cast into amorphous parts [9]. Furthermore, it contains no toxic elements, precious metals, or rare-earth metals, making it the perfect candidate for industrial production.

Different processing technologies however require different alloy properties, especially regarding the crystallization behavior of the alloy, as the onset of crystallization during processing limits the application and processability. When casting parts from the liquid state, the crystallization behavior upon cooling needs to be considered, as the crystallization sequence and kinetics limit the obtainable part size according to the critical casting thickness. On the other hand, when additive manufacturing techniques like selective laser melting are used to print amorphous parts [10–13], these part-size limitations can be bypassed. In this case however, crystallization of the initially amorphous layers in the heat-affected zone needs to be avoided. This process displays a completely different crystallization behavior than the one observed upon cooling.

One way to alter the crystallization behavior of BMGs is microalloying [14,15]. Minor additions of certain elements are added to a known alloy composition, changing the crystallization sequence and kinetics. In the last years, our group discovered sulfur as a constituent in BMGs [16–20], allowing for a large variety of new approaches for alloy development. It was also found that additions of sulfur significantly improve the thermal stability of Vit105 upon heating [16].

Based on this finding, the influence on the crystallization behavior of Vit105 is investigated in depth in this work, using modern *in situ* synchrotron x-ray diffraction experiments. These are conducted both upon heating from the glassy state and upon cooling from the liquid state during electrostatic levitation. The experiments show that the addition of sulfur changes the crystallization sequence and phases, increases the thermal stability upon heating, and decreases the glass-forming ability upon cooling.

II. EXPERIMENT METHODS

The master alloys for Vit105 ($Zr_{52.5}Cu_{17.9}Ni_{14.6}Al_{10}Ti_5$) and its sulfur-containing modification Vit105 S_2 ($Zr_{51.45}Cu_{17.54}Ni_{14.31}Al_{9.8}Ti_{4.9}S_2$) were synthesized from high-purity raw elements with purities above 99.95 wt. %. In the case of Vit105 S_2, a $Ni_{55}S_{45}$ prealloy was used in order to add sulfur to the alloy, as described in Ref. [18]. The constituents were alloyed in an arc-melting furnace under a high-purity Ti-gettered argon atmosphere. To obtain homogeneous master alloys, samples were flipped and remelted at least three times. Amorphous samples were cast in an arc-melting furnace with a suction casting inset,

*benedikt.bochtler@uni-saarland.de

producing rods with a length of 50 mm and a diameter of 3 mm.

Calorimetric measurements were performed using a Perkin-Elmer DSC 8500 for temperatures up to 1000 K and a NETZSCH STA 449 Jupiter DTA for temperatures up to 1400 K. In both cases, the devices were calibrated using the melting transitions of various metals and the measurements took place under a constant flow of ultrahigh-purity Ar and with a heating rate of 0.33 K/s. For melting experiments, Y_2O_3-coated graphite crucibles were used to avoid crucible reactions.

The crystallization behavior was investigated using *in situ* x-ray diffraction experiments. Solid amorphous samples were analyzed upon heating on the PETRA III high-resolution beamline P02.1 at the German Electron Synchrotron (DESY) [21]. As-cast samples were cut to a thickness of around 300 μm and were investigated in transmission mode using a Perkin-Elmer XRD 1621 CsI-bonded amorphous silicon flat-panel detector (2048 × 2048 pixels). A beam size of $0.5 \times 0.5\,\mathrm{mm}^2$ with a wavelength of 0.207 Å (60 keV) was used. The samples were heated from room temperature to 823 K with a constant heating rate of 0.33 K/s in a Linkam THMS 600 furnace under a constant flow of high-purity Ar. Additionally, isothermal experiments at elevated temperatures were conducted where the samples were initially heated with a rate of 2 K/s. Two-dimensional raw diffraction patterns were collected in 10-s intervals.

The crystallization behavior of liquid samples upon cooling was investigated by *in situ* synchrotron x-ray scattering experiments on levitating droplets on the materials science beamline ID11 at the European Synchrotron Radiation Facility (ESRF) [22] and P07 at DESY [23]. Samples were processed in an electrostatic levitation (ESL) device [24–27], where they were levitated in an electrostatic field under high vacuum and could be heated and melted by infrared ($\lambda = 808\,\mathrm{nm}$) lasers. The sample mass was around 100 mg for the ESL experiments. In this setup, highly reactive samples could be processed containerless in the liquid state, thus avoiding reactions and heterogeneous crystallization. An x-ray beam with a size of $0.5 \times 0.5\,\mathrm{mm}^2$ and a wavelength of 0.124 Å (100 keV) was used. At ESRF, the diffraction patterns were recorded by a two-dimensional FReLoN detector (2048 × 2048 pixels), and at DESY by the Perkin-Elmer detector mentioned above, and raw diffraction patterns were collected every second. Samples were heated to several hundred kelvin above the liquidus temperature and then cooled freely. The temperature calibration of the pyrometer was obtained from the melting point upon heating.

For all scattering experiments, the scattering intensity $I(Q)$ was obtained from an azimuthal integration of the diffraction patterns after subtraction of the dark image and the background. The diffraction patterns of the observed crystalline phases were simulated using the software POWDERCELL 2.3 [28].

III. RESULTS AND DISCUSSION

In this work, the crystallization behavior upon heating from the amorphous state and upon cooling from the equilibrium liquid state is investigated and compared for two alloy compositions: Vit105 ($Zr_{52.5}Cu_{17.9}Ni_{14.6}Al_{10}Ti_5$) and its sulfur-containing modification Vit105 S_2 ($Zr_{51.45}Cu_{17.54}Ni_{14.31}Al_{9.8}Ti_{4.9}S_2$).

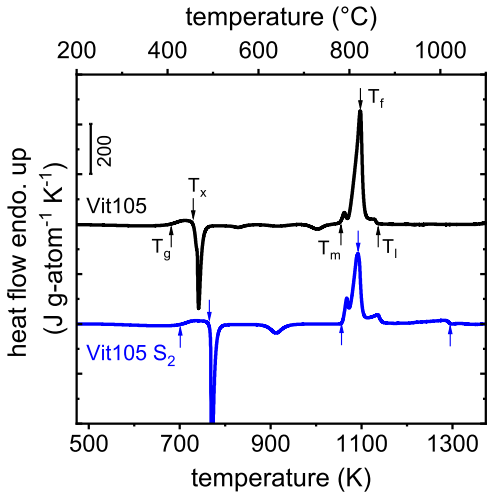

FIG. 1. DTA heating curves for Vit105 and Vit105 S_2 at a heating rate of $q_h = 0.33\,\mathrm{K/s}$. The following characteristic temperatures are indicated by arrows: glass transition temperature T_g, crystallization temperature T_x, melting (or eutectic) temperature T_m, temperature of fusion T_f, liquidus temperature T_l. The corresponding values can be found in Table I.

A. Calorimetry

It has previously been shown by us [16] that minor additions of sulfur result in a significant expansion of the supercooled liquid (SCL) region of Vit105 upon heating, where the maximum expansion is observed at a concentration of 2 at. %. The differential thermal analysis (DTA) curves for Vit105 and Vit105 S_2 upon heating from the glassy state with a rate of 0.33 K/s are displayed in Fig. 1. First, the glass transition is observed at the glass transition temperature T_g, followed by an exothermic crystallization event at the crystallization temperature T_x. The endothermic melting event starts at the melting temperature T_m and is completed when reaching the liquidus temperature T_l. All characteristic temperatures are indicated by arrows in Fig. 1 and are summarized in Table I.

Due to the S addition, the onset of the glass transition temperature T_g is shifted from 671 to 692 K, and the length of the SCL region (ΔT_x) increases from 60 to 77 K, indicating a substantial stabilization of the SCL region. When looking at

TABLE I. Characteristic temperatures, determined by DSC and DTA measurements at a heating rate of $q_h = 0.33\,\mathrm{K/s}$. Glass transition temperature T_g, crystallization temperature T_x, length of the SCL region ΔT_x, melting (or eutectic) temperature for an amorphous sample T_m^{am}, a crystalline sample T_m^{xtal}, temperature of fusion T_f, liquidus temperature T_l.

Alloy	T_g (K)	T_x (K)	ΔT_x (K)	T_m^{am} (K)	T_m^{xtal} (K)	T_f (K)	T_l (K)
Vit105	671.4	731.1	59.7	1055	1071	1095	1134
Vit105 S_2	691.9	769.3	77.4	1057	1065	1093	1295

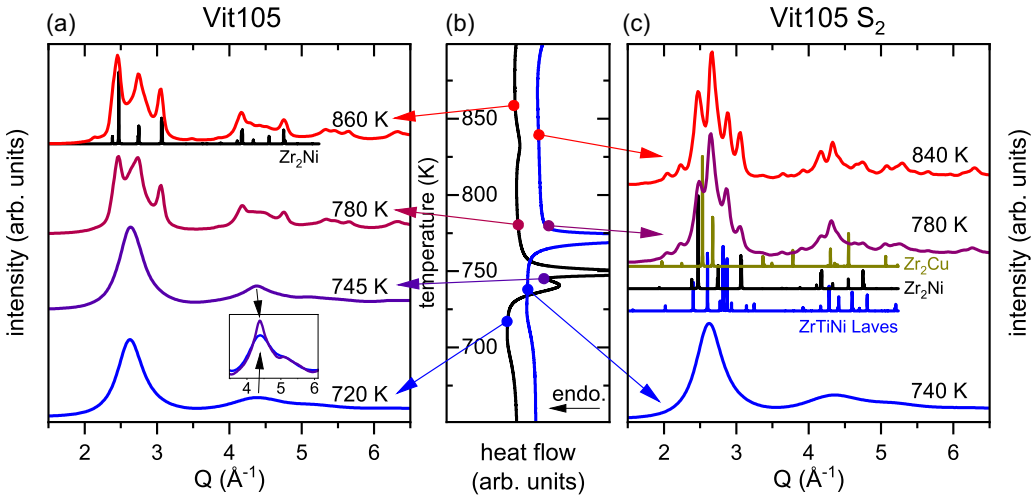

FIG. 2. Crystallization behavior upon heating from the glassy state. *In situ* synchrotron x-ray diffraction patterns of (a) Vit105 and (c) Vit105 S_2 at different temperatures. (b) Vertical DSC scan with the same heating rate of 0.33 K/s as a temperature reference.

the melting behavior, the DTA measurements display a pronounced melting shoulder for Vit105 S_2, causing an increase of the liquidus temperature T_l to 1295 K, while Vit105 almost shows a eutectic composition with $T_l = 1134$ K.

B. X-ray diffraction upon heating

The results of the *in situ* x-ray diffraction experiments upon heating initially amorphous samples are displayed in Fig. 2, elucidating the structural changes during the crystallization process. Figures 2(a) and 2(c) show the scattering intensity $I(Q)$ of Vit105 and Vit105 S_2 at different temperatures. In the center panel [Fig. 2(b)], the corresponding differential scanning calorimetry (DSC) scans with the same heating rate of 0.33 K/s are displayed vertically as a temperature reference. This shows that the diffraction patterns have been selected in accordance with the crystallization events visible in the DSC scan.

The simulated diffraction patterns of the formed crystalline phases are displayed below the experiment data. The corresponding phase is written directly next to the pattern. Due to compositional deviations from the ideal crystalline phase, e.g., due to a substitution with different atom species, the diffraction peaks do not always perfectly coincide with the simulated peaks.

Comparing the crystallization sequence in the DSC signal, Vit105 shows an additional shoulder on the low-temperature side of the principal crystallization peak. The phase separation and crystallization behavior of amorphous Vit105 upon heating and annealing was previously investigated by Johnson and co-workers [29–31]. They used small-angle neutron scattering, transmission electron microscopy, laboratory x-ray diffraction (XRD), and DSC. Their efforts showed that Vit105 decomposes on the nanometer scale, followed by the formation of nanocrystals (roughly with a size of 2 nm) in an amorphous matrix. This event is correlated with the first exothermic event in the DSC scan, drastically reducing the stability of the SCL region. They further conclude that the thermal parameter ΔT_x is not correlated with the GFA for alloys that display phase separation [29].

Based on our diffraction measurements, we observe structural changes and no clear primary crystallization in Vit105 during the exothermic shoulder on the low-temperature side of the principal crystallization peak. The inset in Fig. 2(a) shows a sharpening of the second amorphous halo in the diffraction pattern; however, the possibly forming nanocrystals are so small that no clear Bragg diffraction patterns appear. The nature of the first exothermic shoulder will be discussed later in the context of Fig. 3. The shoulder is immediately followed by a more pronounced crystallization event, where the formation of tetragonal Zr_2Ni crystals is observed. The Zr_2Ni phase remains the dominant one, accounting for all detected Bragg peaks. This fits well to the composition of Vit105, when Ni and Cu are both considered to occupy the Ni sites, due to their topological similarity, and Al and Ti are not considered separately.

The crystallization sequence of Vit105 S_2 is shown in Fig. 2(c). At the onset of crystallization, first, the formation of a ZrTiNi Laves phase is detected, which is confirmed by the isothermal experiments shown later in Fig. 3. The hexagonal lattice structure of the ZrTiNi Laves phase can be formed by different atomic compositions, with one possible composition being $Ti_{45}Zr_{38}Ni_{17}$ [32]. Other compositions can be achieved by an occupation of the lattice sites by different atom species. During the same crystallization event, the subsequent formation of the tetragonal Zr_2Ni and Zr_2Cu phase is observed. In general, the addition of sulfur impedes the onset of crystallization and extends the supercooled liquid region in comparison to the base alloy.

Diffraction patterns of isothermal annealing experiments are presented in Fig. 3. The samples were heated with a rate of 2 K/s from room temperature to the annealing temperature and then annealed for the displayed time. The diffraction patterns are color coded from blue to red for increasing time. In the main panel of each plot, selected diffraction patterns at different times are displayed and the final diffraction pattern after heating the sample to 820 K is shown in black as a

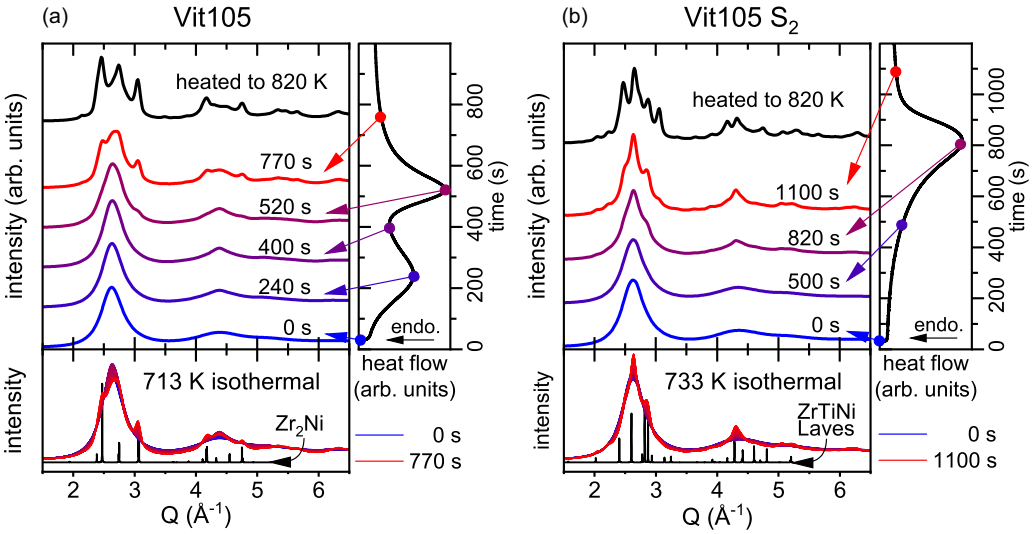

FIG. 3. Isothermal crystallization behavior from the glassy state. *In situ* synchrotron x-ray diffraction patterns of (a) Vit105 and (b) Vit105 S_2. On the right site of the panel, the heat flow during isothermal DSC measurements is displayed as a time reference. On the bottom, all diffraction patterns are displayed one on top of the other, visualizing the development of the diffraction peaks with time.

reference. In the right window, the corresponding isothermal DSC measurement is given as a time reference. In the bottom window, all recorded patterns for the observed time range are displayed on top of each other, again with a color coding from blue to red for increasing times. The exact sequence of the growth of the diffraction peaks can be observed and additionally the calculated diffraction pattern of the primary crystalline phase is shown.

Figure 3(b) shows the isothermal crystallization sequence of Vit105 S_2 at 733 K. In the DSC measurement, only a single exothermic event is visible, and the diffraction patterns also indicate the formation of a single phase. The patterns correspond well to the previously discussed ZrTiNi Laves phase, confirming it as primary crystallizing phase in Vit105 S_2. Only after subsequent heating of the sample up to 820 K, the formation of the tetragonal Zr_2Ni and Zr_2Cu phase is observed, resulting in the same diffraction pattern as obtained from the experiments with a constant heating rate.

In contrast, Vit105 shows a different crystallization behavior, as displayed in Fig. 3(a) for an annealing temperature of 713 K. In isothermal experiments, the shoulder on the low-temperature side of the principal crystallization peak in the DSC scan can be clearly separated from the main peak, as visible in the DSC measurement on the right side. The diffraction patterns up to an annealing time of 400 s show no diffraction peaks, indicating an amorphous or nanocrystalline sample even though the first exothermic event was already completed. This observation coincides well with the results of Johnson and co-workers [29–31], where the first exothermic event corresponds only to chemical decomposition and the beginning of nanocrystallization. The second exothermic event clearly corresponds to the formation of tetragonal Zr_2Ni crystals.

Consequently, one can conclude that chemical decomposition and the beginning of nanocrystallization in Vit105 is suppressed by the addition of sulfur. The primary crystallizing phase upon heating from the glassy state changes and an increase in thermal stability of the modified alloy can be observed.

C. X-ray diffraction during electrostatic levitation

On the other side, when looking into the GFA of an alloy, the crystallization behavior of the metallic liquids upon cooling is the decisive property. However, neither calorimetric cooling experiments nor *ex situ* diffraction experiments on (partially) crystalline samples can resolve the exact crystallization sequence. In the following, experimental results from *in situ* synchrotron x-ray diffraction and ESL are combined to answer this question.

First, the heating and cooling temperature cycles in the synchrotron ESL setup and the obtained diffraction data for a Vit105 S_2 sample are exemplarily presented in Fig. 4. The left panel of Fig. 4 shows *in situ* synchrotron x-ray diffraction patterns upon heating and melting with a color coding from

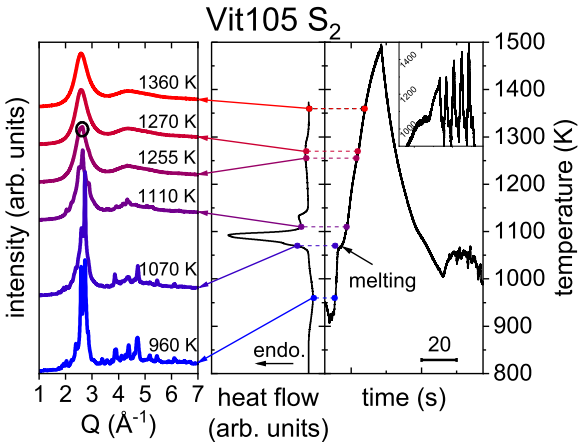

FIG. 4. Heating and melting of a crystalline Vit105 S_2 sample. The left panel shows *in situ* synchrotron x-ray diffraction patterns during ESL. The other panels serve as a temperature reference, with the center one showing a DTA heating curve and the right one displaying the corresponding heating and cooling cycle during the ESL experiments. The inset shows the temperature profile of the whole ESL experiment.

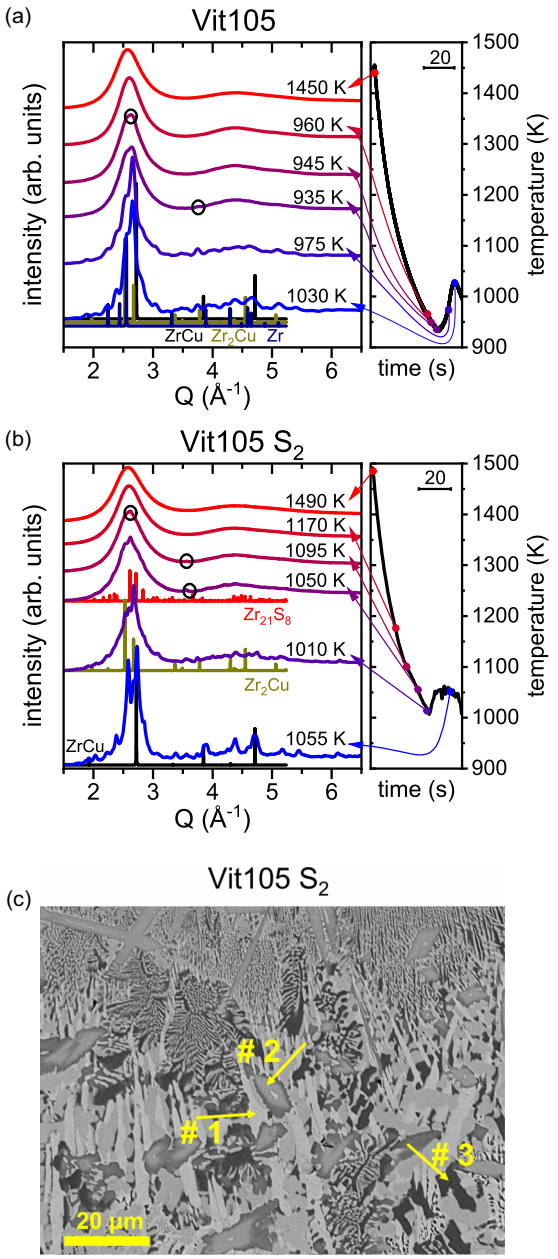

FIG. 5. *In situ* synchrotron x-ray diffraction patterns of (a) Vit105 and (b) Vit105 S_2 for free cooling of a liquid sample during ESL. The temperature profile of the cooling process is shown on the right and the temperature of the displayed diffraction patterns is indicated. (c) Cross-sectional BSE SEM image of the ESL-processed Vit105 S_2 sample. EDX measurements were performed on the three indicated areas.

blue to red for increasing temperatures. In the center panel, a DTA heating curve of a crystalline sample is displayed vertically as a temperature reference. The right panel shows the temperature profile of a single heating and cooling cycle of the ESL experiment, where the left flank corresponds to the displayed diffraction patterns during heating. The right flank relates to the free cooling of the sample, which is discussed in the context of Fig. 5. During cooling, a maximum cooling rate of around −30 K/s is reached. The inset shows the temperature profile of the complete experiment, where five heating and cooling cycles were performed.

The first diffraction pattern at 960 K results from a sample that crystallized previously upon cooling in the ESL, as the critical cooling rate could not be reached. Upon further heating, melting begins at the melting point ($T_m^{\text{xtal}} = 1065$ K) and at 1070 K the intensity of the diffraction peaks already begins to decrease. The melting event is also visible in the ESL temperature profile, where a short isothermal temperature plateau can be seen. After the main melting peak, at 1110 K, the diffraction peaks are already much less pronounced and at 1255 K, right below the liquidus temperature, the sample is almost melted completely and only a weak diffraction peak is visible, as indicated by the circle. At 15 K higher, a completely amorphous liquid structure can be identified.

This observation is in good agreement with the DTA melting curves. The remaining crystalline phase up to 1255 K confirms the observed shoulder in the DTA scan and validates its interpretation as the end of the melting event. The low intensity of the remaining peak further confirms that only a small percentage of the sample remains crystalline to such high temperatures. This melting shoulder at high temperatures is the main difference between Vit105 and Vit105 S_2 in their DTA scans and should therefore result from a sulfur-stabilized phase that does not form in the Vit105 base alloy.

In Fig. 5, the crystallization behavior of (a) Vit105 and (b) Vit105 S_2 upon cooling from the liquid is shown. In the main window of Figs. 5(a) and 5(b), selected diffraction patterns at different temperatures during free cooling are displayed. In the right window, the corresponding ESL temperature profile is plotted. The calculated diffraction patterns of the growing crystalline phases are shown directly below the experimental diffraction pattern.

In the case of Vit105 [Fig. 5(a)], the sample stays fully amorphous down to 960 K, thus reaching an undercooling of 175 K below the liquidus temperature. Crystallization begins at 945 K, where initially only a deformation of the main amorphous diffraction halo is visible (black circle). With the onset of the recalescence, the final diffraction pattern begins to form. The observed peaks can be correlated with a mixture of three crystalline phases, namely the cubic CuZr, the tetragonal Zr_2Cu, and the hexagonal Zr. The observed diffraction pattern of Vit105 upon cooling is different from the pattern formed upon heating an amorphous sample, where a single Zr_2Ni structure is observed, which however is not surprising considering the strongly different time- and length scales of the two different crystallization processes.

The diffraction data for Vit105 S_2 are displayed in Fig. 5(b). First, only minor diffraction peaks become visible at a temperature of 1095 K. Below, at 1050 K, small, humplike diffraction peaks are visible on the amorphous background diffraction signal, indicating a minor fraction of small crystalline particles in the melt. It is plausible that a sulfur-containing phase is formed initially, as sulfur also causes a drastic increase of the liquidus temperature. This is in good agreement with the remaining crystallites at temperatures above the main melting peak observed in the melting experiments in Fig. 4.

Based on the diffraction pattern, the primary phase could possibly be tetragonal $Zr_{21}S_8$. After the formation of this

phase, the formation of the tetragonal Zr_2Cu phase is triggered and the maximum undercooling before the recalescence is much smaller than in Vit105. Hence, the ZrS phase acts as a nucleating agent and reduces the GFA of Vit105 S_2. Additionally, a cubic CuZr phase is formed, which is visible in the final diffraction pattern.

The microstructure of the ESL-processed Vit105 S_2 sample is investigated by scanning electron microscopy (SEM) and energy-dispersive x-ray spectroscopy (EDX). The cross-sectional backscattered electrons (BSE) image is depicted in Fig. 5(c). A fine patterned microstructure is visible. EDX measurements are performed in three differently shaded regions, indicated by yellow arrows. Point No. 1 corresponds to a composition of $Zr_{59}Cu_{22}Ni_{10}Al_5Ti_4$ (in at. %), which is close to the nominal composition, but without sulfur. Phase No. 2 however displays a high concentration of 13 at. % sulfur ($Zr_{61}Cu_7Ni_6Al_{11}Ti_2S_{13}$), but the measured composition cannot clearly be assigned to a binary ZrS compound that could be responsible for the primary crystallization. The darkest phase in BSE contrast at point No. 3 contains a low amount of Zr and has a composition of $Zr_{38}Cu_{15}Ni_{16}Al_{16}Ti_{14}$. The Zr to (Cu/Ni) ratio of almost 1-1 of this phase suggests that it might correspond to the CuZr structure observed in the diffraction patterns.

A reduced GFA for Vit105 S_2 in comparison to Vit105 is also confirmed by casting experiments where the critical casting thickness is determined. In the used experimental suction casting setup, Vit105 displays a critical casting thickness for fully amorphous samples of 8 mm, whereas Vit105 S_2 only reaches 6 mm.

In summary, a Zr_2Cu and a CuZr phase form in both alloys. However, in Vit105 S_2 crystallization is triggered earlier, likely by a ZrS phase, e.g., $Zr_{21}S_8$, which explains the reduced GFA of Vit105 S_2.

D. Time-temperature transformation diagram

When considering the synchrotron XRD experiments upon heating from the glassy state and upon cooling from the liquid state, a complete picture of the crystallization process of Vit105 and Vit105 S_2 can be drawn. The different aspects can be visualized in a time-temperature transformation (TTT) diagram, where the onset of crystallization for a certain temperature is displayed as a function of time. In this depiction, minor additions of sulfur do not simply shift the onset of crystallization to longer or shorter times, but rather change the position of the crystallization nose depending on the temperature region and the dominant crystallization mechanism.

The TTT diagrams for both Vit105 alloys are displayed semischematically in Fig. 6, with black lines corresponding to Vit105 and blue lines to Vit105 S_2. Both liquidus and glass transition temperatures correspond to the calorimetric measurement values. The shape and exact position of the crystallization noses are not fully known; however, the curves are placed in a way that complies with known values from our calorimetric measurements, as well as earlier ESL cooling experiments by Lin *et al.* [6]. The dotted red lines correspond to the temperature protocols of the presented experiments. The cooling curve is taken from the synchrotron ESL experiments and indicates the obtainable undercooling before the onset

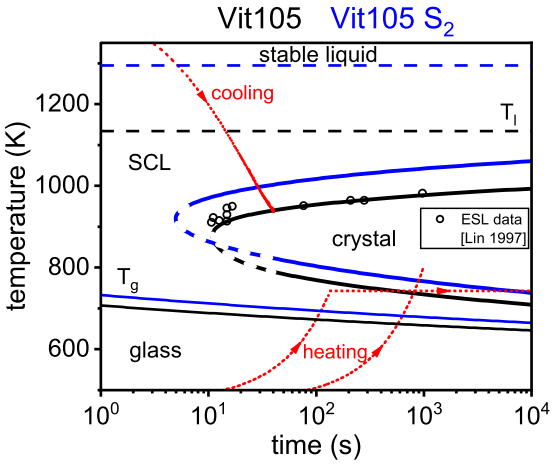

FIG. 6. Semischematic TTT diagram, visualizing the change in the crystallization behavior due to minor additions of sulfur.

of crystallization. The heating curves correspond to a scan with a rate of 0.33 K/s and isothermal measurements with a previous heating rate of 2 K/s. The interrupted parts of the crystallization nose indicate the temperature region which was not experimentally investigated and where the change in the primary phase between the high- and low-temperature regime takes place.

As the addition of sulfur impedes the chemical decomposition and the beginning of nanocrystallization that is observed in Vit105 upon heating, the thermal stability of the SCL region in the low-temperature regime is increased with sulfur, and the onset of crystallization is shifted to longer times. The reduced GFA of Vit105 S_2 upon cooling from the liquid state is reflected by the shorter minimum time until the onset of crystallization. A faster cooling rate is necessary to bypass crystallization and obtain a fully amorphous sample. In the high-temperature regime, a higher crystallization temperature is displayed for Vit105 S_2, which corresponds roughly to the main crystallization event that causes the recalescence in the ESL cooling experiments. The observed formation of a primary ZrS phase that facilitates the main crystallization is not indicated due to its difficult to detect nature.

IV. CONCLUSIONS

In conclusion, additions of sulfur in the Vit105 alloy family cause a change in the crystallization sequence and can be used to fine-tune the crystallization behavior in different temperature regions. While sulfur facilitates crystallization at high temperatures upon cooling from the liquid state in Vit105, it impedes crystallization at low temperatures upon heating from the glassy state in the same system. With a profound knowledge of the primary phases and their influence on the crystallization kinetics, one can tailor the alloy according to the needs of specific applications.

While for the casting of larger amorphous parts, the unmodified Vit105 alloy is advantageous, the Vit105 S_2 alloy provides an increased thermal stability upon heating, e.g., for processing via selective laser melting [12,13], or thermoplastic forming [33–35], where crystallization of the glassy phase needs to be avoided.

ACKNOWLEDGMENTS

The authors acknowledge the possibility to perform high-energy synchrotron XRD experiments at the light source Petra III at the DESY in Hamburg and at the ESRF in Grenoble. This research was supported by the German Research Foundation (DFG) through Grants No. BU 2276/10-1, No. BU 2276/11-1, and No. ME 1958/12-1. Furthermore, we are grateful to Maximilian Frey, Nico Neuber, Zach Evenson, Moritz Stolpe, Shuai Wei, Isabell Jonas, Dirk Holland-Moritz, Sandro Szabó, and Dandan Zhao for their support during the various beamtimes.

[1] C. Schuh, T. Hufnagel, and U. Ramamurty, Mechanical behavior of amorphous alloys, Acta Mater. **55**, 4067 (2007).

[2] M. M. Trexler and N. N. Thadhani, Mechanical properties of bulk metallic glasses, Prog. Mater Sci. **55**, 759 (2010).

[3] C. T. Liu, M. F. Chisholm, and M. K. Miller, Oxygen impurity and microalloying effect in a Zr-based bulk metallic glass alloy, Intermetallics **10**, 1105 (2002).

[4] G. Kumar, T. Ohkubo, and K. Hono, Effect of melt temperature on the mechanical properties of bulk metallic glasses, J. Mater. Res. **24**, 2353 (2009).

[5] D. Grell, J. Gibmeier, S. Dietrich, F. Silze, L. Böhme, V. Schulze, U. Kühn, and E. Kerscher, Influence of shot peening on the mechanical properties of bulk amorphous Vitreloy 105, Surf. Eng. **33**, 721 (2017).

[6] X. H. Lin, W. L. Johnson, and W. K. Rhim, Effect of oxygen impurity on crystallization of an undercooled bulk glass forming alloy, Mater. Trans. JIM **38**, 473 (1997).

[7] W. L. Johnson, J. H. Na, and M. D. Demetriou, Quantifying the origin of metallic glass formation, Nat. Commun. **7**, 10313 (2016).

[8] N. D. Campos Neto, C. Soares, F. S. Pereira, V. Bergamaschi, S. G. Antonio, M. J. Kaufman, and M. F. de Oliveira, Glass forming ability and continuous-cooling-transformation (CCT) diagrams of Vitreloy 105 as function of cooling rate and oxygen concentration, J. Non Cryst. Solids **528**, 119762 (2020).

[9] L. Liu, T. Zhang, Z. Liu, C. Yu, X. Dong, L. He, K. Gao, X. Zhu, W. Li, C. Wang, P. Li, L. Zhang, and L. Li, Near-net forming complex shaped Zr-based bulk metallic glasses by high pressure die casting, Materials **11**, 2338 (2018).

[10] S. Pauly, L. Löber, R. Petters, M. Stoica, S. Scudino, U. Kühn, and J. Eckert, Processing metallic glasses by selective laser melting, Mater. Today **16**, 37 (2013).

[11] X. P. Li, M. P. Roberts, S. O'Keeffe, and T. B. Sercombe, Selective laser melting of Zr-based bulk metallic glasses: Processing, microstructure and mechanical properties, Mater. Des. **112**, 217 (2016).

[12] S. Pauly, C. Schricker, S. Scudino, L. Deng, and U. Kühn, Processing a glass-forming Zr-Based alloy by selective laser melting, Mater. Des. **135**, 133 (2017).

[13] M. Frey, J. Wegner, N. Neuber, B. Reiplinger, B. Bochtler, B. Adam, L. Ruschel, S. S. Riegler, H.-R. Jiang, S. Kleszczynski, G. Witt, and R. Busch, Thermoplastic forming of additively manufactured Zr-based bulk metallic glass: a processing route for surface finishing of complex structures, Mater. Des. **198**, 109368 (2021).

[14] W. H. Wang, Roles of minor additions in formation and properties of bulk metallic glasses, Prog. Mater Sci. **52**, 540 (2007).

[15] Z. P. Lu and C. T. Liu, Role of minor alloying additions in formation of bulk metallic glasses: a review, J. Mater. Sci. **39**, 3965 (2004).

[16] A. Kuball, O. Gross, B. Bochtler, and R. Busch, Sulfur-bearing metallic glasses: A new family of bulk glass-forming alloys, Scr. Mater. **146**, 73 (2018).

[17] A. Kuball, O. Gross, B. Bochtler, B. Adam, L. Ruschel, M. Zamanzade, and R. Busch, Development and characterization of titanium-based bulk metallic glasses, J. Alloys Compd. **790**, 337 (2019).

[18] A. Kuball, B. Bochtler, O. Gross, V. Pacheco, M. Stolpe, S. Hechler, and R. Busch, On the bulk glass formation in the ternary Pd-Ni-S system, Acta Mater. **158**, 13 (2018).

[19] O. Gross, L. Ruschel, A. Kuball, B. Bochtler, B. Adam, and R. Busch, Bulk metallic glass formation in the (Ti,Zr)–(Ni,Cu)–S system, J. Phys.: Condens. Matter **32**, 264003 (2020).

[20] J. Wilden, F. Yang, D. Holland-Moritz, S. Szabó, W. Lohstroh, B. Bochtler, R. Busch, and A. Meyer, Impact of sulfur on the melt dynamics of glass forming $Ti_{75}Ni_{25-x}S_x$, Appl. Phys. Lett. **117**, 013702 (2020).

[21] A.-C. Dippel, H.-P. Liermann, J. T. Delitz, P. Walter, H. Schulte-Schrepping, O. H. Seeck, and H. Franz, Beamline P02.1 at PETRA III for high-resolution and high-energy powder diffraction, J. Synchrotron Radiat. **22**, 675 (2015).

[22] A. Bernasconi, J. Wright, and N. Harker, Total scattering experiments on glass and crystalline materials at the ESRF on the ID11 beamline, Powder Diffract. **30**, S2 (2015).

[23] N. Schell, A. King, F. Beckmann, T. Fischer, M. Müller, and A. Schreyer, The high energy materials science beamline (HEMS) at PETRA III, Mater. Sci. Forum **772**, 57 (2013).

[24] W. Rhim, S. K. Chung, D. Barber, K. F. Man, G. Gutt, A. Rulison, and R. E. Spjut, An electrostatic levitator for high-temperature containerless materials processing in 1-g, Rev. Sci. Instrum. **64**, 2961 (1993).

[25] W.-K. Rhim, K. Ohsaka, P.-F. Paradis, and R. E. Spjut, Noncontact technique for measuring surface tension and viscosity of molten materials using high temperature electrostatic levitation, Rev. Sci. Instrum. **70**, 2796 (1999).

[26] T. Meister, H. Werner, G. Lohoefer, D. M. Herlach, and H. Unbehauen, Gain-scheduled control of an electrostatic levitator, Control Eng. Pract. **11**, 117 (2003).

[27] T. Kordel, D. Holland-Moritz, F. Yang, J. Peters, T. Unruh, T. Hansen, and A. Meyer, Neutron scattering experiments on liquid droplets using electrostatic levitation, Phys. Rev. B **83**, 104205 (2011).

[28] W. Kraus and G. Nolze, POWDER CELL – a program for the representation and manipulation of crystal structures and calculation of the resulting X-ray powder patterns, J. Appl. Crystallogr. **29**, 301 (1996).

[29] A. A. Kündig, J. F. Löffler, and W. L. Johnson, Composition dependence of phase separation and crystallization in deeply undercooled Zr-(Ti-)Cu-Ni-Al alloys, MRS Proc. **644**, L5.6 (2000).

[30] J. F. Löffler, S. Bossuyt, S. C. Glade, W. L. Johnson, W. Wagner, and P. Thiyagarajan, Crystallization of bulk amorphous Zr–Ti(Nb)–Cu–Ni–Al, Appl. Phys. Lett. **77**, 525 (2000).

[31] E. Pekarskaya, J. F. Löffler, and W. L. Johnson, Microstructural studies of crystallization of a Zr-Based bulk metallic glass, Acta Mater. **51**, 4045 (2003).

[32] P. Villars (chief editor), $Ti_{45}Zr_{38}Ni_{17}$ (ZrTiNi) Crystal Structure, *PAULING FILE in: Inorganic Solid Phases* (Springer, Heidelberg, 2016), https://materials.springer.com/isp/crystallographic/docs/sd_1803780.

[33] J. Schroers, Processing of bulk metallic glass, Adv. Mater. **22**, 1566 (2010).

[34] W. L. Johnson, G. Kaltenboeck, M. D. Demetriou, J. P. Schramm, X. Liu, K. Samwer, C. P. Kim, and D. C. Hofmann, Beating crystallization in glass-forming metals by millisecond heating and processing, Science **332**, 828 (2011).

[35] B. Bochtler, O. Kruse, and R. Busch, Thermoplastic forming of amorphous metals, J. Phys.: Condens. Matter **32**, 244002 (2020).